

The variability of the broad-line Balmer decrement for quasars from the Sloan Digital Sky Survey Reverberation Mapping

Yan-Song Ma¹, Shao-Jun Li¹, Chen-Sheng Gu¹, Jian-Xia Jiang¹, Kai-Li Hou¹, Shu-Hao Qin¹, Wei-Hao Bian¹ *

¹*School of Physics and Technology, Nanjing Normal University, Nanjing 210023, People's Republic of China*

9 May 2023

ABSTRACT

Based on the spectral decomposition through a code of PrepSpec, the light curves (spanning 6.5 years in the observed frame) of the broad-line Balmer decrement, i.e., the flux ratio of the broad H α to the broad H β line, are calculated for a sample of 44 Sloan Digital Sky Survey reverberation-mapped quasars ($z < 0.53$). It is found that the logarithm of the mean broad-line Balmer decrement is 0.62 with a standard deviation of 0.15 dex. The relations between the mean Balmer decrement and the SMBH accretion properties (the luminosity, black hole mass, Eddington ratio, accretion rate) are investigated and no obvious correlations are found. It is found that there are 27 quasars (61%) showing strong negative correlations between the Balmer decrement variance and the continuum variance, i.e., the Balmer decrement would be smaller with larger continuum flux. Assuming that the dust obscuration leads to the variance in the Balmer decrement and the continuum, an expected slope is $-1/3$, which is not consistent with most of measured slopes. Using the interpolated cross-correlation function, the time delays between the inverse Balmer decrement and the continuum are measured for 14 quasars with the maximum correlation coefficient larger than 0.6. It suggests that the size corresponding to the Balmer decrement lag extends from the BLR size to the torus size.

Key words: galaxies: active – quasars: emission lines – quasars: general – quasars: supermassive black holes

1 INTRODUCTION

Active galactic nuclei (AGN) are accreting supermassive black holes (SMBHs) at the centres of galaxies. The standard paradigm for AGN assumes that the central SMBH is surrounded by an accretion disc (AD) and broad-line region (BLR), which are surrounded by a dusty torus, and a farther narrow-line region (NLR). The NLR/BLR Balmer decrement ($H\alpha/H\beta$) is usually used as a tool to investigate the properties of gas and dust in AGN (e.g., Brinchmann et al. 2004; Osterbrock & Ferland 2006; Lu et al. 2019b).

Predicted by Case B recombination (at a typical low electron density of 10^2 cm^{-3} and temperature of 10^4 K), an intrinsic Balmer decrement value of 2.86 is suggested for H II region photoionized by a hot star. For Balmer decrement of AGN, a larger value for the intrinsic decrement is predicted from CLOUDY code, where is due to the presence of NLR/BLR gas of higher densities, much harder ionizing continuum, lower ionization parameter (Osterbrock & Ferland 2006; Netzer 2013; Heard & Gaskell 2016).

The distributions of Balmer decrement of NLR/BLR were reported for different selected AGN samples (e.g., Dong et al. 2005, 2008; Heard & Gaskell 2016; Baron et al. 2016; Lu et al. 2019b). For a sample of blue AGN defined by the spectral slopes in order to minimize the effect of dust extinction, the distributions of the intrinsic BLR Balmer decrement was investigated (Dong et al. 2008). Based on this sample of extremely blue AGN, Gaskell (2017) suggested that the intrinsic Balmer is 2.72 ± 0.041 , which is consistent

with the Case B value of 2.74 (Osterbrock & Ferland 2006). The small scatter of 0.04 dex suggested the BLR decrement can be used a reddening indicator for the BLR, as well as for the NLR decrement (e.g., Dong et al. 2008; Bian et al. 2010a; Heard & Gaskell 2016; Lu et al. 2019b). For a compiled sample of AGN with reliable decomposition of the narrow/broad H α /H β lines (Osterbrock 1977; Cohen 1983; Dong et al. 2005, 2008), it was also found that the average BLR Balmer decrement is larger than NLR (Heard & Gaskell 2016), suggesting an additional dust reddening the BLR is interior to the NLR, which is possibly due to the dust in BLR and/or in torus. However, this is opposite to the results obtained by others, (de Zotti & Gaskell 1985; Dong et al. 2008; Baron et al. 2016; Lu et al. 2019b). The comparison between the NLR and BLR Balmer decrement depends on the method to de-composite the BLR/NLR contribution in H α and H β lines.

For quasars from the Sloan Digital Sky Survey (SDSS), it was found that BLR Balmer decrement depends on the optical continuum slope, although with a larger scatter (see Fig. 7 in Baron et al. 2016). It was also found that there is no correlation between the decrement and the luminosity (Dong et al. 2008; Lu et al. 2019b). Recently the variability of the BLR Balmer decrement is investigated for individual AGN (e.g., Siram et al. 2021; Pandas & Seigowska 2022; Li et al. 2022; Selwood et al. 2023). The Balmer decrement variability for a sample with spectral monitoring would provide clues to these problems.

It was suggested that the diversity of AGN can be unified by the orientation and the Eddington ratio (Shen & Ho 2014). It is necessary to investigate the relation between the BLR/NLR decrement and the accretion process. For broad-line AGN, the BLR clouds (size

* E-mail: whbian@njnu.edu.cn

R_{BLR} and velocity ΔV) can be used as a probe to calculate its virial mass as follows (e.g., Peterson et al. 2004; Yu et al. 2020b):

$$M_{\text{BH}} = f \times \frac{R_{\text{BLR}} (\Delta V)^2}{G}, \quad (1)$$

where G is the gravitational constant, f is a virial factor. From the standard disk model of Shakura & Sunyaev (1973), the dimensionless accretion rate $\dot{\mathcal{M}}$ can be calculated from L_{5100} and M_{BH} as follows (e.g., Du et al. 2016):

$$\dot{\mathcal{M}} \equiv \dot{M}/\dot{M}_{\text{Edd}} = 20.1 \left(\frac{l_{44}}{\cos i} \right)^{3/2} m_7^{-2}, \quad (2)$$

where \dot{M} is the accretion rate, the Eddington accretion rate $\dot{M}_{\text{Edd}} = L_{\text{Edd}}/c^2$, $l_{44} = L_{5100}/10^{44} \text{ erg s}^{-1}$ is the 5100 Å luminosity in units of $10^{44} \text{ erg s}^{-1}$, L_{Edd} is the Eddington luminosity, $m_7 = M_{\text{BH}}/10^7 M_{\odot}$ is the SMBH mass in units of $10^7 M_{\odot}$, i is the accretion disk inclination relative to the observer and $\cos i = 0.75$. The Eddington ratio $L_{\text{Bol}}/L_{\text{Edd}}$ and the dimensionless accretion rate $\dot{\mathcal{M}}$ are two important parameters describing the SMBH accretion process, where L_{Bol} is the bolometric luminosity. Considering $L_{\text{Bol}} = \eta \dot{M} c^2$, where η is the accretion efficiency, $L_{\text{Bol}}/L_{\text{Edd}} = \frac{\eta \dot{M} c^2}{M_{\text{Edd}} c^2} = \eta \dot{\mathcal{M}}$.

In this paper, for a sample of 44 SDSS-RM quasars, we use light curves (spanning 6.5 years) of $\text{H}\beta$, $\text{H}\alpha$ and the continuum at 5100 Å derived from the spectral decomposition through PrepSpec to investigate the variability of BLR Balmer decrement ($\text{H}\alpha/\text{H}\beta$). In Section 2, we describe the sample and light curve data. The mean value of the Balmer decrement and its connection with the SMBH accretion, the relative variance of the Balmer decrement, the relation of $\text{H}\alpha/\text{H}\beta$ variability with the continuum, and the lag of the Balmer decrement with respect to the continuum are presented in Section 3. Section 4 is our results.

2 SAMPLE

SDSS-RM Project monitored a flux-limited ($i_{\text{psf}} < 21.7$) sample of 849 quasars with redshifts of $0.1 < z < 4.5$ on the 2.5 m SDSS telescope with the BOSS spectrograph (Shen et al. 2016; Grier et al. 2017). The wavelength coverage of BOSS spectra is $\sim 3650\text{--}10400\text{Å}$ with a spectral resolution of $R \sim 2000$. Additional photometric data were acquired with the 3.6 m Canada–France–Hawaii Telescope (CFHT) and the Steward Observatory 2.3 m Bok telescope.

A code called PrepSpec¹ is used to improve the relative flux calibrations and produce line/continuum light curves (Shen et al. 2016; Grier et al. 2017; Khatu et al. 2023). What PrepSpec does is similar to the decomposition approach used in other studies (e.g., Bian et al. 2010b; Barth et al. 2015; Hu et al. 2015, 2021). Because we use the light curves derived from PrepSpec, the code is introduced as follows. For each SDSS-RM spectrum for an RM quasar, the PrepSpec model is: $\mu(\lambda, t) = p(t)[A(\lambda, t) + B(\lambda, t) + C(\lambda, t)]$, where $p(t)$ are time-dependent photometric corrections, $A(\lambda)$ is the average spectrum, and $B(\lambda, t)$ and $C(\lambda, t)$ are variations in the BLR spectrum and continuum, respectively. $A(\lambda) = \bar{F}(\lambda) + N(\lambda)$, where $\bar{F}(\lambda)$ includes both the continuum and broad-line components, as well as the Fe II pseudo-continuum (host-galaxy light is not included). The narrow-line component, $N(\lambda)$, is isolated using a

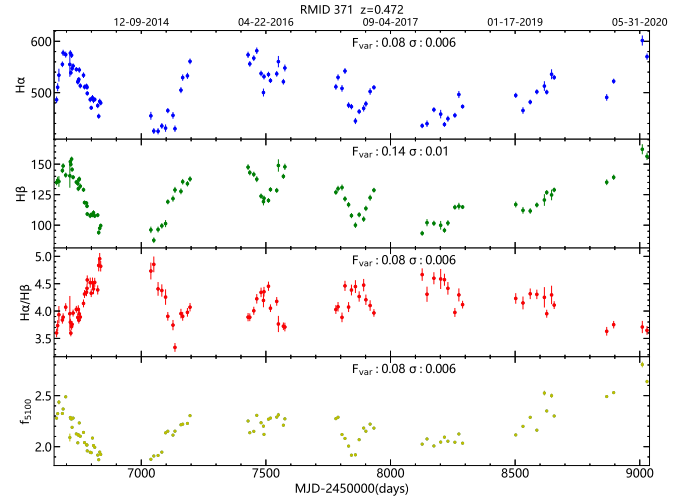


Figure 1. Light curves of the $\text{H}\alpha$, $\text{H}\beta$, $\text{H}\alpha/\text{H}\beta$, continuum at 5100 Å (from top to bottom) for an example of quasar, SDSS J141123.42+521331.7 (RMID 0371, $z = 0.472$). The relative variance and its error for each light curve are shown in the upper middle corner of each panel.

piecewise cubic spline fit to $A(\lambda)$ as a high-pass filter and then multiplying the result by a window function that is 0 outside and 1 inside a defined velocity range around a specified list of narrow emission lines. The BLR variations $B(\lambda, t)$ are represented by a separable function for each line, $B(\lambda, t) = \sum_{l=1}^{N_l} B_l(\lambda) L_l(t)$, where the light curve $L_l(t)$ is normalized to a mean of 0 and rms of 1, and $B_l(\lambda)$ is the rms spectrum of line l . A key feature of PrepSpec is the inclusion of a time-dependent flux correction calculated by assuming that there is no intrinsic variability of the narrow emission-line fluxes. PrepSpec minimizes the apparent variability of the narrow lines by fitting a model to the spectra that includes intrinsic variations in both the continuum and different broad emission lines. The narrow-line and broad-line window widths are determined through iterating until convergence in PrepSpec. It is different to other decomposition methods using multi-Gaussians for one by one spectrum (e.g., Bian et al. 2010b; Barth et al. 2015; Hu et al. 2015, 2021).

The light curves of $\text{H}\beta$, $\text{H}\alpha$, and the continuum derived from PrepSpec model for 44 quasars ($z < 0.53$) are given in the website of Keith Horne². Because the long coverage of light curves (MJD from 2456660 to 2459029, about 6.5 years) and the updated spectral analysis, we use the data provided by the website of Keith Horne instead of the data shown in Table 2 in Grier et al. (2017)³. The observation cadence (average sampling interval of the objects) is large, about 5 days in the years of 2014, about 13 days in years of 2015–2017, and about 20 days in years of 2018–2020. The sample of these 44 SDSS-RM quasars is used to investigate the Balmer decrement $\text{H}\alpha/\text{H}\beta$.

Figure 1 shows an example of the light curve of the Balmer decrement, as well as the $\text{H}\alpha$, $\text{H}\beta$ and the continuum at 5100 Å for one quasar (RMID 0371, $z = 0.472$). For the light curve of $\text{H}\alpha/\text{H}\beta$, the ratio of $\text{H}\alpha$ to $\text{H}\beta$ emission line flux is calculated from the website of Keith Horne. Through the error propagation formula, errors of

¹ PrepSpec: <https://github.com/Alymantara/pyPrepSpec>

² <http://star-www.st-and.ac.uk/~kdh1/pub/sdss/2020/sdssz.html>

³ <https://cdsarc.cds.unistra.fr/ftp/J/ApJ/851/21/>

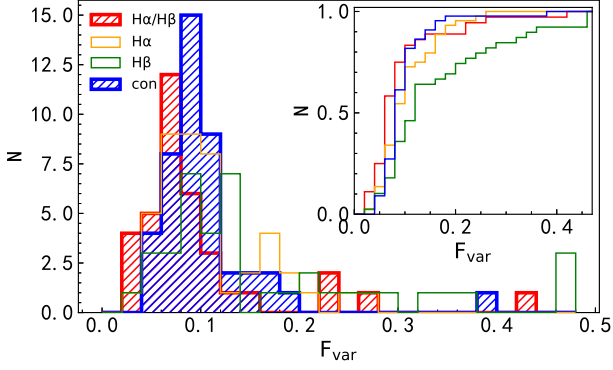


Figure 2. Distribution of F_{var} for $\text{H}\alpha/\text{H}\beta$ (filled with red lines), the continuum at 5100 \AA (filled with blue lines), $\text{H}\alpha$ (orange lines) and $\text{H}\beta$ (green lines). The inserted panel in the upper right corner shows the corresponding cumulative distribution of F_{var} .

$\text{H}\alpha$ and $\text{H}\beta$ flux are used to calculate the error of $\text{H}\alpha/\text{H}\beta$,

$$\sigma = \frac{f_{\text{H}\alpha}}{f_{\text{H}\beta}} \sqrt{(\sigma_{\text{H}\beta}/f_{\text{H}\beta})^2 + (\sigma_{\text{H}\alpha}/f_{\text{H}\alpha})^2} \quad (3)$$

where σ is the error of Balmer decrement, $f_{\text{H}\alpha}$ and $f_{\text{H}\beta}$ are the emission fluxes of $\text{H}\alpha$ and $\text{H}\beta$, $\sigma_{\text{H}\alpha}$ and $\sigma_{\text{H}\beta}$ are the corresponding errors of $\text{H}\alpha$ and $\text{H}\beta$.

3 RESULTS AND DISCUSSIONS

3.1 The relative variance of the Balmer decrement $\text{H}\alpha/\text{H}\beta$

Accounting for the measurement uncertainties, the relative intrinsic variability amplitude F_{var} is used to show the variance in the light curve. F_{var} and its uncertainty $\sigma_{F_{\text{var}}}$ of a light curve are as commonly defined (e.g., Rodriguez-Pascual et al. 1997; Edelson et al. 2002; Fausnaugh et al. 2016; Lu et al. 2019a; Zhao et al. 2020):

$$F_{\text{var}} = \frac{(\sigma^2 - \Delta^2)^{1/2}}{\bar{f}}, \quad \sigma_{F_{\text{var}}} = \frac{1}{F_{\text{var}}} \left(\frac{1}{2N}\right)^{1/2} \frac{\sigma^2}{\bar{f}}, \quad (4)$$

where \bar{f} is the average flux of f_i , σ is the standard deviation of flux f_i , N is the number of observations, Δ^2 is the mean square of uncertainty Δ_i on the flux f_i . F_{var} gives an estimate of the relative intrinsic variability amplitude by accounting for the measurement uncertainties.

For each light curve, we calculate the relative intrinsic variability amplitude F_{var} and its error, where are presented in Table 1. There are 7 quasars without values of F_{var} because of Δ^2 larger than σ^2 . Figure 2 is the F_{var} distribution of the broad-line Balmer decrement $\text{H}\alpha/\text{H}\beta$, as well as $\text{H}\alpha$, $\text{H}\beta$ and continuum at 5100 \AA for our sample. The mean F_{var} of $\text{H}\alpha/\text{H}\beta$ is 0.11 ± 0.019 , the mean F_{var} of $\text{H}\alpha$ of all sample is 0.11 ± 0.009 , the mean F_{var} of $\text{H}\beta$ is 0.22 ± 0.023 , and the mean F_{var} of continuum is 0.10 ± 0.008 . The mean F_{var} of $\text{H}\alpha/\text{H}\beta$ is similar to $\text{H}\alpha$ and the continuum, but smaller than $\text{H}\beta$.

Kolmogorov–Smirnov (K–S) test⁴ is performed to investigate the distribution differences among them. For the distributions of the decrement $\text{H}\alpha/\text{H}\beta$ and $\text{H}\alpha$, K-S test shows the statistic d and the

⁴ We used python (scipy.stats.ks_2samp, scipy.stats.spearmanr) to do our following analysis for the K-S test and the Spearman correlation test.

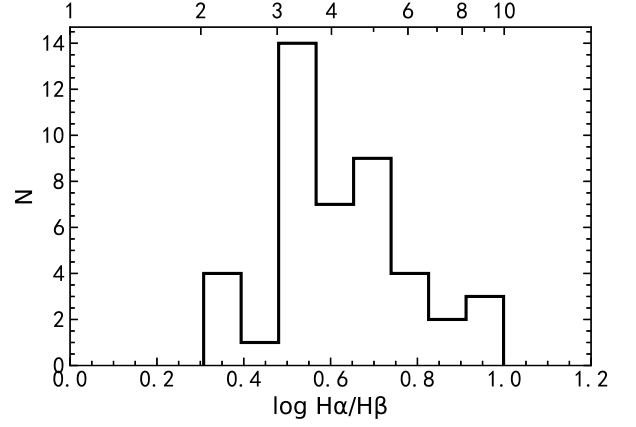


Figure 3. The distribution of the mean Balmer decrement ($\log \text{H}\alpha/\text{H}\beta$) showing a large range from 0.3 to 1.

significant level probability for the null hypothesis (p) are 0.23 and 0.20. It shows that there are no obvious difference between their distributions. It is the case for the distributions of $\text{H}\alpha/\text{H}\beta$ and continuum at 5100 \AA with $d=0.24$ and $p = 0.17$. For the distributions of $\text{H}\alpha/\text{H}\beta$ and $\text{H}\beta$, $d=0.46$ and $p = 2 \times 10^{-4}$, which showing the difference between their distributions.

3.2 The mean value of $\text{H}\alpha/\text{H}\beta$ and the relation with the SMBH accretion

For each quasar, we use the square of the measurement error as the weight to calculate the mean value of $\text{H}\alpha/\text{H}\beta$. The error of the mean $\text{H}\alpha/\text{H}\beta$ is calculated from the weighted mean of the measurement errors and the weighted standard deviation. Figure 3 shows the distribution of the mean Balmer decrement $\log(\text{H}\alpha/\text{H}\beta)$. The mean value of $\log(\text{H}\alpha/\text{H}\beta)$ is 0.62 with the standard deviation of 0.15 dex. For $\text{H}\alpha/\text{H}\beta$, the mean value is 4.17 with the standard deviation of 1.42. We notice that our measured BLR $\text{H}\alpha/\text{H}\beta$ have a larger range extending from 2 to 10. It is found that the BLR $\text{H}\alpha/\text{H}\beta$ has a strong relation with the equivalent width (EW) of the broad $\text{H}\beta$ line ($r_s = -0.43$, $p_{\text{null}} = 4.0 \times 10^{-3}$), while no obvious relation with $\text{H}\alpha$ EW ($r_s = 0.073$, $p_{\text{null}} = 0.64$). It is possible that the large $\text{H}\alpha/\text{H}\beta$ is due to weak $\text{H}\beta$ line. Therefore, if we excluding quasars with $\text{H}\beta(\text{EW}) < 20$, the mean $\log \text{H}\alpha/\text{H}\beta$ is 0.57 with the standard deviation of 0.11 dex, i.e., 3.71 ± 0.90 for the mean $\text{H}\alpha/\text{H}\beta$. For BLR $\text{H}\alpha/\text{H}\beta$, its value changes from one sample to another. Dong et al. (2008) found it is 3.06, Gaskell (2017) suggested it is 2.72 and Lu et al. (2019b) found it is 3.16. However, Lakicevic et al. (2017) found it is 3.76, as well as 3.38 found by Siram et al. (2021). Our result is similar to that by Lakicevic et al. (2017).

For quasars with reliable lag detection (Grier et al. 2017), M_{BH} is adopted from col. (11) in Table 1 from Yu et al. (2020b), as well as its error, which is calculated from the broad $\text{H}\beta$ line dispersion from the rms spectrum and the lag suggested by (Grier et al. 2017). For other quasars, considering the extended empirical $R_{\text{BLR}}(\text{H}\beta) - L_{5100}$ relation including R_{Fe} (Du & Wang 2019; Yu et al. 2020a), M_{BH} is calculated as follows: $\log \frac{M_{\text{BH}}}{M_{\odot}} = 7.01 + 2 \log \frac{\text{FWHM}_{\text{H}\beta}}{1000 \text{ km/s}} + 0.48 \log l_{44} - 0.38 R_{\text{Fe}}$ (Liu & Bian 2022), where l_{44} , $\text{FWHM}_{\text{H}\beta}$ and optical R_{Fe} are measured from the mean spectra (Shen et al. 2019). Based on the error transfer formula, the error of M_{BH} is cal-

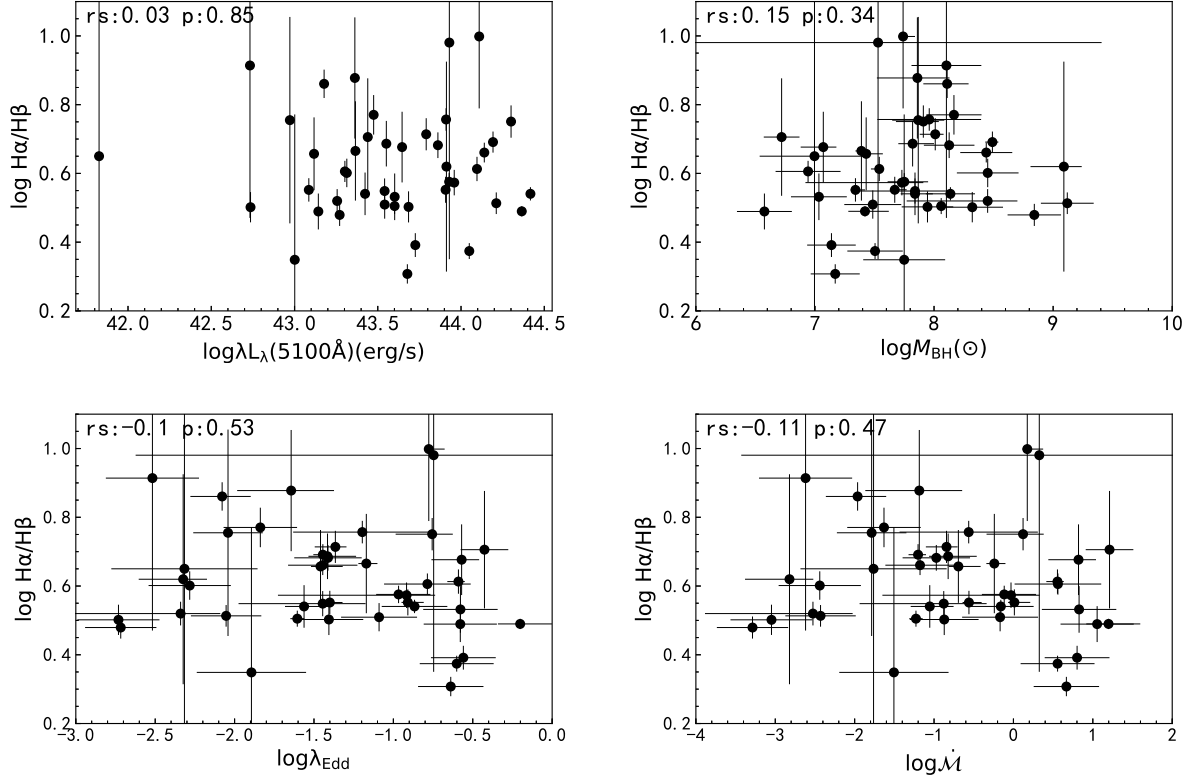


Figure 4. The relations of the mean Balmer decrement with the the continuum L_{5100} (top left), the SMBH mass M_{BH} (top right), the Eddington ratio $L_{\text{Bol}}/L_{\text{Edd}}$ (bottom left) and the dimensionless accretion rate \dot{M} (bottom right). The Spearman test result is shown in the top corner in each panel.

culated from the errors of $\text{FWHM}_{\text{H}\beta}$, L_{5100} , R_{Fe} , including a systematic error of 0.2 dex for $R_{\text{BLR}}(\text{H}\beta)$. The error of \dot{M} is about double M_{BH} error. The error of $L_{\text{Bol}}/L_{\text{Edd}}$ is about 0.33 dex (e.g., Liu & Bian 2022; Chen et al. 2022).

In Table 1, L_{5100} , $\text{FWHM}_{\text{H}\beta}$, R_{Fe} , M_{BH} are shown in cols. (14-17). Sulentic et al. (2000) proposed two main populations on the plane of $\text{FWHM}_{\text{H}\beta}$ versus R_{Fe} (Shen & Ho 2014): Population A (Pop. A) for quasars with $\text{FWHM}_{\text{H}\beta} < 4000 \text{ km s}^{-1}$ and Population B (Pop. B) for those with $\text{FWHM}_{\text{H}\beta} > 4000 \text{ km s}^{-1}$. For our sample, there are 23 quasars belong to Pop. B, 21 quasars belong to Pop. A and 5 quasars belong to extreme Pop. A with $R_{\text{Fe}} > 1.2$.

In Figure 4, we show the relations of the mean value of $\text{H}\alpha/\text{H}\beta$ with L_{5100} , M_{BH} , $L_{\text{Bol}}/L_{\text{Edd}}$ and \dot{M} . There is a large M_{BH} error bar for RMID 0767, which is due to its large error of $\text{FWHM}_{\text{H}\beta}$, i.e., $2003 \pm 3868 \text{ km s}^{-1}$. It seems that there exists a trend of smaller $\text{H}\alpha/\text{H}\beta$ with larger L_{5100} and $L_{\text{Bol}}/L_{\text{Edd}}$ or \dot{M} . Using the Spearman correlation test to investigate the correlations between the mean Balmer decrement and L_{5100} , M_{BH} , $L_{\text{Bol}}/L_{\text{Edd}}$, \dot{M} . The test coefficient r_s and the probability of the null hypothesis p_{null} are 0.03, 0.85 for L_{5100} , 0.15 and 0.34 for M_{BH} , -0.1 and 0.53 for $L_{\text{Bol}}/L_{\text{Edd}}$, -0.11 and 0.47 for \dot{M} . No obvious correlations are found between the mean Balmer decrement and the L_{5100} , M_{BH} , $L_{\text{Bol}}/L_{\text{Edd}}$, \dot{M} .

3.3 The relation between the Balmer decrement variance and the continuum variance at 5100 Å

It was suggested that there existed a correlation between $\text{H}\alpha/\text{H}\beta$ and the continuum for a single AGN (e.g., Siram et al. 2021;

Pandas & Seigowska 2022; Li et al. 2022). Figure 5 shows an example of the relation between the variance of the Balmer decrement $\text{H}\alpha/\text{H}\beta$ and the variance of the continuum at 5100 Å for one quasar (RMID 0371). There exists a strong correlation with $r_s = -0.65$ and $p_{\text{null}} = 5.8 \times 10^{-12}$. Its continuum changes about 0.2 dex, and its decrement changes about 0.18 dex. Considering the errors in both coordinates, through kmpfit⁵, the best linear fit is $\log \text{H}\alpha/\text{H}\beta = -(0.68 \pm 0.03) \log f_{\text{con}} + (0.84 \pm 0.01)$. The fitting slope is -0.68 ± 0.03 , which would be test by the dust obscuration (see next paragraph). In the bottom panel in Figure 5, we also show the continuum at 5100 Å versus the continuum flux at g+i band for the spectra at the year of 2014 (Grier et al. 2017). The relation between them is strong with $r_s = 0.92$. The linear fitting slope by kmpfit is 1.038 ± 0.037 . Although existing line-contribution at g+i band, the slope of 1.038 shows the spectral continuum fluxes are consistent well with the photometric continuum fluxes at g+i band.

For all 44 quasars in our sample, the correlation coefficient r_s , p_{null} and the fitting slope k are given in Cols. (11-13) in Table 1. For the r_s distribution, the mean value of the total sample is -0.45 and the standard deviation is 0.78. In Figure 6, we show p_{null} versus r_s , as well their histograms in the top and right panel. The orange shaded region shows the $p_{\text{null}} \geq 0.01$. Considering $p_{\text{null}} < 0.01$, there are about 61% (27/44) quasars showing obvious anti-correlation. There is only one quasar with $r_s > 0$ with $p_{\text{null}} < 0.01$. For the subsample with $p_{\text{null}} < 0.01$, the mean value of r_s is -0.55 with a standard deviation of 0.16.

It is generally believed that Balmer decrements can be used for

⁵ <https://www.astro.rug.nl/software/kapteyn/kmpfittutorial.html>.

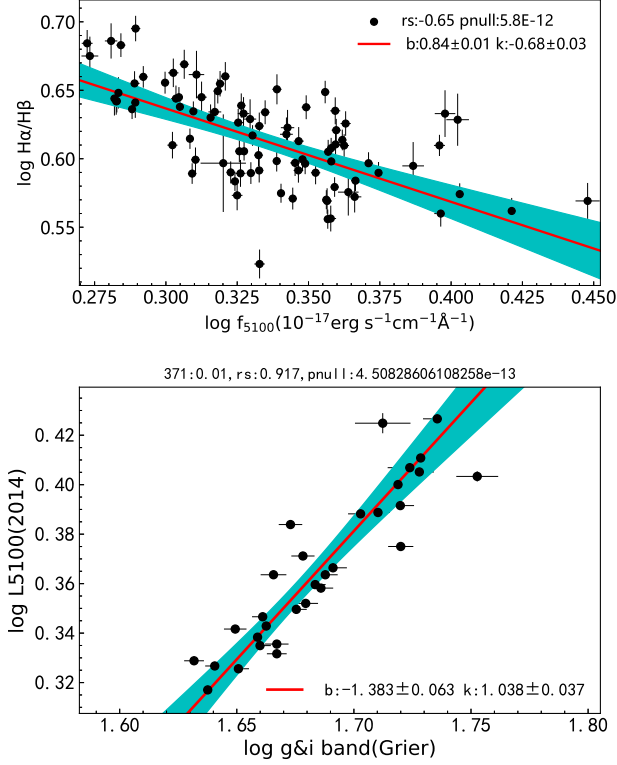


Figure 5. Top: the relationship between $H\alpha/H\beta$ and continuum spectral flux for an example of quasar, SDSS J141123.42+521331.7 (RMID 0371, $z = 0.472$). The red solid line is the best linear fitting and the blue region is the confidence band. Bottom: the continuum at 5100 \AA versus the continuum flux at g+i band for the spectra at the year of 2014 (Grier et al. 2017) for this quasar. The red line and the blue region are the same as in the top panel.

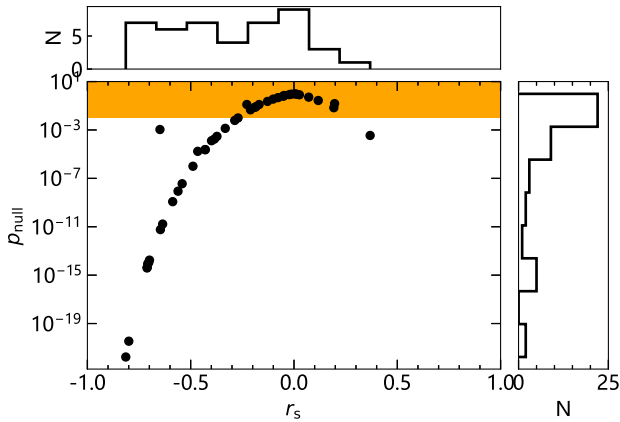


Figure 6. The distribution of the Spearman correlation coefficient r_s versus the distribution of probability of the null hypothesis p_{null} . The orange shaded region shows $p_{\text{null}} \geq 0.01$, indicating no strong correlation.

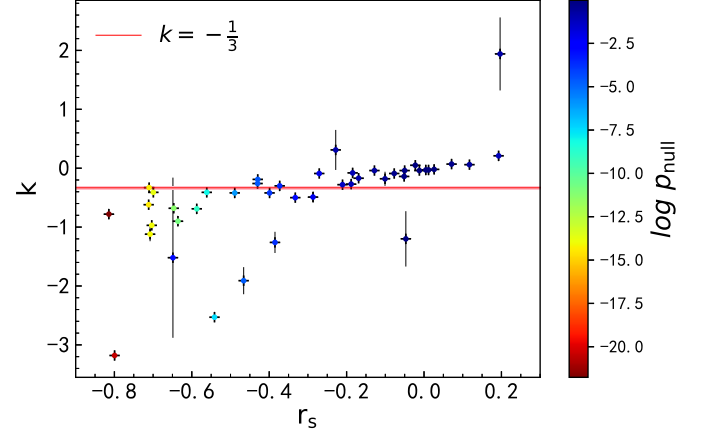


Figure 7. The slope versus r_s for the relation between the Balmer decrement and continuum flux at 5100 \AA . The color bar shows the p_{null} from the Spearman test. The red solid line shows the theoretical value of slope ($k = -1/3$) predicted from the extinction and the constant continuum/line flux.

dust extinction. The extinction at the wavelength of λ can be calculated using the formula: $\langle A(\lambda)/A(V) \rangle = a(x) + b(x)/R_V$, where $x \equiv 1/\lambda$. According to the definition of extinction, $A(\lambda) = m_\lambda^{\text{obs}} - m_\lambda^{\text{int}} = -2.5 \log \frac{f_\lambda^{\text{obs}}}{f_\lambda^{\text{int}}}$, where $m_\lambda^{\text{obs}}, m_\lambda^{\text{int}}$ are the observed and intrinsic magnitude, $f_\lambda^{\text{obs}}, f_\lambda^{\text{int}}$ are the observed and intrinsic flux. Therefore, at the wavelength of $\lambda = 5100 \text{ \AA}$:

$$f_{5100}^{\text{int}} = f_{5100}^{\text{obs}} \left[\frac{\left(\frac{H\alpha}{H\beta} \right)^{\text{obs}}}{\left(\frac{H\alpha}{H\beta} \right)^{\text{int}}} \right]^{\frac{A(5100\text{\AA})}{A(H\beta) - A(H\alpha)}} \quad (5)$$

Using the extinction law of the Milky Way with $R_V = 3.1$, it is found that $A(5100\text{\AA}) = 1.11/A_V$, $A(H\alpha) = 1.18/A_V$, $A(H\beta) = 0.81/A_V$. We obtain the index in Eq. 5 is 3.

Assuming the variance in $H\alpha/H\beta$ and the continuum is coming from the dust extinction, i.e., the intrinsic $H\alpha/H\beta$ and the continuum are stable, from Eq. 5, a relation can be found: $\Delta(\log H\alpha/H\beta) \propto -\frac{1}{3} \Delta(\log L_{5100})$, i.e., a slope of $-1/3$. Figure 7 shows the slope k versus r_s , as well as the color bar based on p_{null} . Red solid line shows the line of $k = -1/3$ predicted from the obscuration and the pink shaded area shows the 10% uncertainty. Considering error of 10%, there are only 4 quasars consistent with the slope of $-1/3$. Most of our measured slopes are not consistent with the expected value of $-1/3$ derived from the dust obscuration. It implies that there exists intrinsic variance of the continuum and the line flux.

3.4 The lag of the Balmer decrement

Because of the anti-correlation between $H\alpha/H\beta$ and the continuum, we calculate the light curve of the inverse $H\alpha/H\beta$, i.e., $\log H\beta/H\alpha$, and use the common methods to detect the lag with respect to the continuum ($\log f_{\text{con}}$). There are mainly three methods to do that, the interpolated cross-correlation function (ICCF) (e.g., Peterson et al. 2004), JAVELIN (Zu et al. 2011, 2013), and CREAM (Starkey et al. 2016). ICCF is the most common method to measure time lags between two light curves in AGN (e.g., Peterson et al.

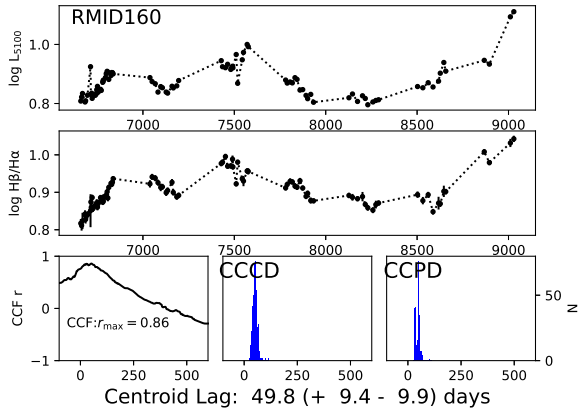


Figure 8. Light curves and CCF model for the the inverse of $H\alpha/H\beta$ analysis for an example of a quasar, SDSS J141041.25+531849.0 (RMID 0160, $z = 0.359$). The light curves of the continuum ($\log f_{\text{con}}$) and the inverse of the broad-line Balmer decrement ($\log H\beta/H\alpha$) (vertically shifted to assure positive values) are presented in the top and middle panels. For display purposes, we show the weighted mean of all epochs observed within a single night. The bottom three panels show the results of the time-series analysis. The bottom left panel shows the CCF. The other two panels present the lag distributions for the two different methods, normalized to the tallest peak in the distribution. The bottom middle panel shows the CCCD, the bottom right panel shows the CCPD lag distribution. For RMID 0160, the lag is $49.8^{+9.4}_{-9.9}$ light days.

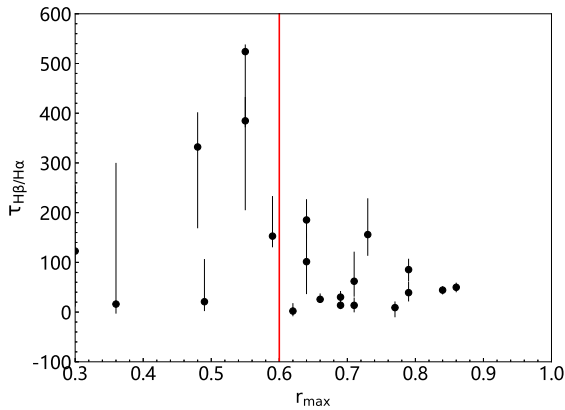


Figure 9. Lag of the Balmer decrement $\tau_{\text{cent}}(H\beta/H\alpha)$ versus the maximum correlation coefficient r_{max} for light curves obtained in years of 2014-2020. The red line shows $r_{\text{max}} = 0.6$.

2004; Bian et al. 2010b; Grier et al. 2017). For 26 quasars with reliable measurement of $H\beta$ or $H\alpha$ lag given by Grier et al. (2017), from light curves of $H\alpha/H\beta$ and the continuum at 5100 \AA , we calculate CCFs and centroid lag τ_{cent} using an interpolation grid spacing of 2 days, and a time lag limiting to a range between -100 and 600 days. The centroid lag is measured using points surrounding the maximum correlation coefficient r_{max} out to $r \geq 0.8r_{\text{max}}$, as is standard for CCF analysis (e.g., Peterson et al. 2004; Grier et al. 2017). The lag of the Balmer decrement is listed in col. 22 in Table 2.

Figure 8 shows an example about the CCF analysis for the light curves of $H\beta/H\alpha$ and the continuum at 5100 \AA for years of 2014-

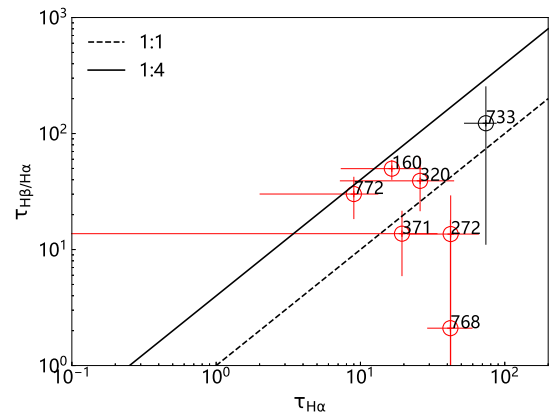
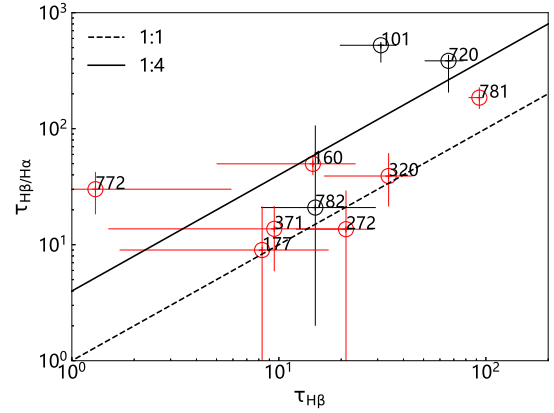


Figure 10. Comparison between the $H\alpha/H\beta$ lag and the $H\beta$ lag (top), the $H\alpha$ lag (bottom). The dot line is 1:1, and the solid line is 1:4 for the size ratio of BLR to the torus. The red circles denote quasars with $r_{\text{max}} > 0.6$. The labels near locations of data points are quasars RMID.

2020 for SDSS J141041.25+531849.0 (RMID 0160, $z = 0.359$). The light curves of the continuum and $H\beta/H\alpha$ are presented in the top and middle panels. For display purposes, we show the weighted mean of all epochs observed within a single night. The bottom three panels show the results of the time-series analysis. The bottom left panel shows the CCF. With the increasing lag, the correlation coefficient reach the maximum ($r_{\text{max}} = 0.86$) at about 49.8 light days, and then slow down with weak correlation. The other two panels present the lag distributions from the two different methods, cross-correlation centroid distribution (CCCDD) and cross-correlation peak distribution (CCPD).

Figure 9 shows the lag τ_{cent} of the Balmer decrement versus the maximum correlation coefficient r_{max} for light curves obtained in years of 2014-2020. The Balmer decrement lags are removed for quasars with $r_{\text{max}} < 0.3$ as not significant. The maximum ICCF correlation coefficient, r_{max} , was suggested to be greater than 0.45. This ensures that the behaviour in the two light curves is well correlated (Grier et al. 2017). Adopting $r_{\text{max}} > 0.6$, there are 14 out of 26 quasars showing a reliable measurement of τ_{cent} .

For SDSS RM quasars, the observation numbers are about 32, 12, 13, 12, 9, 8, 4 during seven years from 2014 to 2020. Considering the larger gaps between adjacent years (see Figure 1), we also do the ICCF analysis for other two cases, one is for the spectra observed during the year of 2014, and the other is during years of 2014-2015.

For our sample, the results on τ_{cent} and r_{max} for the Balmer decrement, as well as $H\beta$, $H\alpha$ from ICCF are given in cols. (6-11) and cols. (12-17), cols. (18-23) in Table 2 for the year of 2014, for years of 2014-2015 and for years of 2014-2020, respectively. Comparing the decrement lag in three cases, i. e., 2014, 2014-2015, 2014-2020, it is found that, for the light curves obtained in the year of 2014, the decrement lag has large uncertainty. With all data in the years of 2014 to 2020, the decrement lag has small uncertainty. It is possible due to small amount of data for ICCF (about 30 data points). Therefore, we use the decrement lag measurement from the data during seven years from 2014 to 2020 (about 90 data points).

Balmer decrement is obtained as the ratio of fluxes of $H\alpha$ and $H\beta$, which have different lags as the response to the continuum light curve. The curve obtained from the ratio of $H\alpha$ and $H\beta$ may represent the curve of the one with the larger amplitudes. It is possible that the Balmer decrement lag is false if the decrement lag is similar to the lag of the $H\beta$ or $H\alpha$. Comparing our measured $H\beta$ lags with the decrement lags through ICCF from light curves obtained during the years of 2014-2020, it is found that there are ten quasars showing obvious lag difference (considering lag errors). For the case of our measured $H\alpha$ lags and the decrement lags through ICCF, there are 12 quasars showing obvious lag difference (considering lag errors). The subsample of these 12 quasars is used to investigate the relation between the decrement lag and the BLR lag.

The RM program gave empirical BLR $R_{\text{BLR}}(H\beta) - L_{5100}$ relation (Peterson et al. 2004; Bentz et al. 2013; Du & Wang 2019; Yu et al. 2020a). Yang et al. (2020) used infrared WISE W1 data to measure the torus size and gave the torus R-L relation. The torus size is about 4 times of the BLR size. Considering our smaller numbers of the continuum data points and large gaps between adjacent years, we use the lag results for $H\beta$ and $H\alpha$ from Grier et al. (2017). In Figure 10, we compare the Balmer decrement lag and the $H\beta$ lag (top), or the $H\alpha$ lag (bottom). Red circles denote quasars with $r_{\text{max}} > 0.6$. The solid line is 1:4, i.e., $\tau_{H\alpha/H\beta} = 4\tau_{H\beta}$ (or $\tau_{H\alpha}$) and the dash line is 1:1. There are larger uncertainties in the decrement lags, $H\beta$, or $H\alpha$ lags. For the top panel in Figure 10, i.e., the decrement lag versus the $H\beta$ lag, there are 3 quasars located above the line of 1:4, 6 quasars located between two lines of 1:1 and 1:4, and one quasar located below the line of 1:1. For the bottom panel in Figure 10, i.e., the decrement lag versus the $H\alpha$ lag, there is 4 quasars located between two lines of 1:1 and 1:4, three quasars located below the line of 1:1. From our results, the size corresponding to the Balmer decrement lag extends from the BLR size to the torus size.

We use the data from the spectrum decomposition through PreSpec, the host contribution is not included. It would influence the measurements of the contribution of the AGN continuum, as well as Fe II quasi-continuum (e.g., Bon et al. 2020). This limitations in our data may influence the final results.

4 CONCLUSIONS

For a sample of 44 SDSS RM quasars ($z < 0.53$) with spectral monitoring of $H\beta$ and $H\alpha$ observed from 2014 to 2020 (6.5 years), using the light curves of $H\alpha$, $H\beta$ and the continuum at 5100 Å derived from the spectral decomposition through PreSpec, the variance of $H\beta/H\alpha$ is investigated. The main conclusions can be summarized as follows:

- The logarithm of the mean broad-line Balmer decrement is 0.62 with a standard deviation of 0.15 dex.
- No obvious correlations are found between the mean Balmer

decrement and the SMBH accretion properties, such as the continuum luminosity, the black hole mass, the Eddington ratio, the dimensionless accretion rate.

- There are 27 quasars (61%) showing strong negative correlations between the Balmer decrement and the continuum, i.e., the Balmer decrement would be smaller with larger continuum flux. Assuming that the dust obscuration leads to the variance in the Balmer decrement and the continuum, the expected slope is -1/3, which is not consistent with most of our measured slopes.

- For 26 quasars with reliable measurement of the $H\beta$ and/or $H\alpha$ delay, through ICCF, the time delays between the inverse Balmer decrement and the continuum are measured. Using the maximum correlation coefficient larger than 0.6, reliable decrement lags are detected for 14 quasars. It suggests that the size of the Balmer decrement lag extends from the BLR size to the torus size.

ACKNOWLEDGEMENTS

We are also very grateful to the anonymous referee for her/his instructive comments which significantly improved the content of the paper. This work is supported by the National Key Research and Development Program of China (No. 2017YFA0402703). This work has been supported by the National Science Foundation of China (No. 11973029).

DATA AVAILABILITY

The data underlying this article are available at <http://star-www.st-and.ac.uk/kdh1/pub/sdss/2020/sdssz.html>.

REFERENCES

- Antonucci R., 1993, ARA&A, 31, 473
 Baron D., Stern J., Poznanski D., & Netzer H., 2016, ApJ, 832, 8
 Barth A. J., Bennert V. N., Canalizo G., et al., 2015, ApJS, 217, 26
 Bentz M. C., et al., 2013, ApJ, 767, 149
 Bian W. H., Zhang S. Y. 2010, Sci. China Phys. Mech. Astron., 53 (Suppl 1), 191
 Bian W. H., Huang K., Hu C., et al., 2010, ApJ, 718, 460
 Blandford R., McKee C., 1982, ApJ, 244, 419
 Brinchmann J., 2004, MNRAS, 351, 1151
 Bon N., et al., 2020, A&A, 635, A151
 Cardelli J. A., Clayton G. C., & Mathis J. S., 1989, ApJ, 345, 245
 Chen Y. Q., Liu Y. S., Bian W. H., 2022, ApJ, 940, 50
 Cohen R. D., 1983, ApJ, 273, 489
 de Zotti G., Gaskell C. M., 1985, A&A, 147, 1
 Dong X.-B., Zhou H.-Y., Wang T.-G., Wang J.-X., Li C., Zhou Y.-Y., 2005, ApJ, 620, 629
 Dong X. B., Wang T. G., Wang, J. G., et al., 2008, MNRAS, 383, 581
 Du P., et al., 2016, ApJ, 825, 126
 Du P., Wang J.-M., 2019, ApJ, 886, 42
 Edelson R., Turner T.J., Pounds K., et al., 2002, ApJ, 568, 610
 Fausnaugh M. M., Denney K. D., Barth A. J., et al., 2016, ApJ, 821, 56
 Gaskell C. M., 2017, MNRAS, 467, 226
 Grier C. J., Trump J. R., Shen Y. et al., 2017, ApJ, 851, 21
 Heard C. Z. P. & Gaskell C. M., 2016, MNRAS, 461, 4227
 Hu C., Du P., Lu K. X., et al., 2015, ApJ, 804, 138
 Hu C., Li S. S., Yang S., et al., 2021, ApJS, 253, 20
 Kaspi S., et al., 2000, ApJ, 533, 631
 Khatu V. C. et al., 2023, PASP, in press
 Lakicevic M., Kovacevic-Dojcinovic J., Popovic L. C., 2017, MNRAS, 472, 334

- Liu Y. S. Bian W. H., 2022, ApJ, 937, 82
Lu K. X., et al., 2019a, ApJ, 877, 23
Lu K. X., et al., 2019b, MNRAS, 483, 1722
Netzer H., 2013, *The Physics and Evolution of Active Galactic Nuclei* (Cambridge: Cambridge Univ. Press), P.94
Osterbrock D. E., 1977, ApJ, 215, 733
Osterbrock D. E., Ferland G. J., 2006, *Astrophysics of Gaseous Nebulae and Active Galactic Nuclei*, 2nd edn. University Science Books, Mill Valley, CA
Pandas S., Sniegowska M., 2022, arXiv: 2206.10056
Peterson B. M., 1993, PASP, 105, 247
Peterson B. M., et al., 2004, ApJ, 613, 682
Rodríguez-Pascual P.M., Alloin D., Clavel J., et al., 1997, ApJS, 110, 9
Shakura N. I., Sunyaev R. A., 1973, A&A, 24, 337
Sriam S., Nour D., Choi, C. S., 2021, arXiv: 2112.04180
Li Y. C., et al., 2022, arXiv: 2208.01797
Selwood M., et al., 2023, MNRAS, 518, 130, arXiv:2210.04827
Shen Y., Ho L. C., 2014, Nature, 513, 210
Shen Y., Brandt W. N., Dawson K. S., et al., 2015, ApJS, 216, 4
Shen Y., Horne K., Grier C. J., et al., 2016, ApJ, 818, 30
Shen Y., Hall P. B., Horne K., et al., 2019, ApJS, 241, 34
Starkey D. A., Horne K., Villforth C., 2016, MNRAS, 456, 1960
Sulentic J. W., Marziani P., Dultzin-Hacyan D. 2000, ARA&A, 38, 521
Urry C. M., Padovani P., 1995, PASP, 107, 803
Yang Q., Shen Y., Liu X., 2020, ApJ, 900, 58
Yu L. M., Zhao B. X., Bian W. H., et al., 2020a, MNRAS, 491, 5881
Yu L. M., Bian W. H., Zhang X. G., et al., 2020b, ApJ, 901, 133
Zhao B. X., Bian W. H., Yu L. M., Wang C., 2020, Ap&SS, 365, 22
Zu Y., Kochanek C.S., Peterson B.M., 2011, ApJ735, 80
Zu Y., Kochanek C.S., Kozłowski S., Udalski A., 2013, ApJ, 765, 106

Table 1. The relative variability amplitude for $H\alpha/H\beta$, $H\beta$, $H\alpha$, L_{5100} , as well as the properties for the relation between $H\alpha/H\beta$ and the continuum at 5100 Å and the SMBH masses. Col. (1): RMID, col. (2): redshift; col. (3): the broad Balmer decrement, col. (4): F_{var} of $H\alpha/H\beta$, col. (5): the flux of the broad $H\alpha$ in units of 10^{-17} erg s $^{-1}$ cm $^{-2}$, col. (6): F_{var} of $H\alpha$, col. (7): the flux of the broad $H\beta$ in units of 10^{-17} erg s $^{-1}$ cm $^{-2}$, col. (8): F_{var} of $H\beta$, col. (9): the continuum flux at 5100 Å in 10^{-17} erg s $^{-1}$ cm $^{-2}$ Å $^{-1}$, col. (10): F_{var} of the continuum at 5100 Å, cols. (11-13): r_s , p_{null} , k for the relation between the $H\alpha/H\beta$ and the continuum, cols. (14-17): the luminosity in 5100 Å in units of erg s $^{-1}$, FWHM of broad $H\beta$ line in units of km s $^{-1}$, R_{Fe} and $\log M_{\text{BH}}/M_{\odot}$.

RMID	z	$H\alpha/H\beta$	$F_{\text{var}}(H\alpha/H\beta)$	$H\alpha$	$F_{\text{var}}(H\alpha)$	$H\beta$	$F_{\text{var}}(H\beta)$	f_{5100}	$F_{\text{var}}(f_{5100})$	r_s	p_{null}	k	L_{5100}	FWHM $_{H\beta}$	R_{Fe}	M_{BH}
(1)	(2)	(3)	(4)	(5)	(6)	(7)	(8)	(9)	(10)	(11)	(12)	(13)	(14)	(15)	(16)	(17)
17	0.46	3.58±0.54	-	343.73±36.09	0.25±0.02	54.77±6.33	0.68±0.05	5.28±0.9	0.38±0.03	-0.81	0.0	-0.78±0.02	43.91±0.0	6075.62±121.48	0.67±0.01	9.09 $^{+0.28}_{-0.15}$
85	0.24	3.0±0.33	0.07±0.02	1188.08±129.16	0.12±0.01	384.49±42.82	0.13±0.01	6.29±0.76	0.16±0.01	-0.01	0.91	-0.04±0.01	43.27±0.0	13797.44±363.93	0.26±0.02	8.84 $^{+0.22}_{-0.22}$
88	0.52	4.56±0.51	0.04±0.03	497.95±44.34	0.06±0.01	107.71±12.12	0.09±0.01	2.6±0.31	0.09±0.01	-0.37	0.0	-0.3±0.04	44.14±0.0	5492.04±82.07	0.37±0.03	8.44 $^{+0.22}_{-0.22}$
101	0.46	3.08±0.34	0.03±0.01	1100.52±120.82	0.04±0.0	353.74±39.09	0.04±0.0	4.8±0.58	0.09±0.01	-0.27	0.01	-0.09±0.01	44.36±0.0	2651.7±302.18	0.43±0.04	7.42 $^{+0.14}_{-0.2}$
126	0.19	4.02±0.45	0.06±0.02	461.65±50.66	0.1±0.01	113.84±12.72	0.09±0.01	7.61±0.88	0.06±0.0	-0.05	0.64	-0.04±0.06	43.3±0.0	1879.01±155.38	1.27±0.03	6.94 $^{+0.27}_{-0.27}$
160	0.36	5.09±0.57	0.1±0.04	844.94±89.94	0.16±0.01	153.99±17.03	0.25±0.02	2.15±0.25	0.15±0.01	-0.71	0.0	-0.62±0.02	43.79±0.0	5034.4±34.91	0.3±0.01	8.01 $^{+0.13}_{-0.07}$
177	0.48	3.71±0.44	0.08±0.03	436.59±46.5	0.08±0.01	116.55±13.31	0.14±0.01	2.13±0.27	0.14±0.01	-0.7	0.0	-0.41±0.02	43.96±0.0	5229.7±76.04	0.47±0.02	7.73 $^{+0.81}_{-0.18}$
184	0.19	2.02±0.22	0.06±0.01	830.7±90.81	0.07±0.01	405.1±45.05	0.06±0.0	12.56±1.44	0.08±0.01	-0.13	0.23	-0.04±0.02	43.68±0.0	1837.28±11.06	0.9±0.01	7.17 $^{+0.21}_{-0.21}$
191	0.44	4.58±0.58	0.23±0.12	133.34±15.04	0.22±0.02	27.61±3.29	0.33±0.03	1.59±0.19	0.1±0.01	-0.21	0.05	-0.28±0.08	43.65±0.01	2177.65±43.98	0.65±0.04	7.07 $^{+0.19}_{-0.11}$
229	0.47	4.72±0.56	0.13±0.06	198.06±21.75	0.11±0.01	38.47±4.3	0.24±0.02	1.21±0.14	0.1±0.01	-0.59	0.0	-0.69±0.04	43.55±0.0	4328.84±297.53	0.6±0.03	7.82 $^{+0.12}_{-0.18}$
252	0.28	3.14±0.36	0.08±0.03	352.08±39.12	0.06±0.0	109.28±12.36	0.09±0.01	2.56±0.29	0.05±0.0	-0.29	0.01	-0.49±0.09	42.74±0.01	10565.13±692.7	0.44±0.03	8.32 $^{+0.23}_{-0.26}$
270	0.42	5.84±0.72	-	217.7±25.92	0.09±0.01	37.04±4.46	0.13±0.01	1.52±0.18	0.12±0.01	-0.17	0.13	-0.17±0.06	43.48±0.0	6470.68±181.01	0.89±0.05	8.17 $^{+0.23}_{-0.23}$
272	0.26	3.75±0.41	0.06±0.02	2368.22±258.11	0.07±0.0	620.05±68.34	0.09±0.01	7.74±0.92	0.12±0.01	-0.71	0.0	-0.33±0.01	43.93±0.02	3514.91±17.43	0.33±0.01	7.75 $^{+0.14}_{-0.2}$
305	0.53	4.89±0.55	0.06±0.03	504.81±56.88	0.07±0.01	102.54±11.64	0.08±0.01	2.59±0.32	0.08±0.01	0.01	0.91	-0.03±0.03	44.19±0.0	2917.6±61.7	0.47±0.04	8.49 $^{+0.06}_{-0.05}$
320	0.26	3.41±0.43	0.14±0.04	509.16±57.2	0.11±0.01	145.64±16.99	0.22±0.02	3.69±0.43	0.1±0.01	-0.7	0.0	-0.97±0.04	43.42±0.0	4700.09±54.96	0.67±0.02	7.84 $^{+0.12}_{-0.15}$
338	0.42	6.83±1.06	0.08±0.253	138.23±16.67	0.11±0.01	15.45±1.93	0.37±0.04	1.59±0.19	0.07±0.01	-0.47	0.0	-1.91±0.23	43.36±0.0	6789.45±579.67	0.0±0.0	7.86 $^{+0.34}_{-0.27}$
341	0.42	3.47±0.4	0.04±0.01	1199.25±137.62	0.08±0.01	347.85±39.71	0.1±0.01	5.53±0.69	0.1±0.01	-0.43	0.0	-0.19±0.02	44.42±0.0	3471.49±24.98	0.57±0.01	8.14 $^{+0.21}_{-0.21}$
371	0.47	4.07±0.47	0.08±0.03	506.45±56.22	0.08±0.01	122.14±13.75	0.14±0.01	2.13±0.24	0.08±0.01	-0.65	0.0	-0.68±0.03	44.1±0.0	4105.97±37.6	0.75±0.02	7.54 $^{+0.07}_{-0.04}$
377	0.34	4.49±0.63	0.22±0.46	148.29±16.57	0.17±0.01	30.46±3.71	0.34±0.03	2.44±0.28	0.05±0.0	-0.39	0.0	-1.26±0.18	43.37±0.0	4429.12±105.45	0.95±0.05	7.39 $^{+0.05}_{-0.07}$
497	0.51	3.24±0.37	0.06±0.02	612.98±69.21	0.07±0.01	186.55±21.43	0.03±0.0	3.88±0.46	0.08±0.01	0.0	0.96	-0.03±0.03	44.21±0.0	11162.28±264.83	0.21±0.02	9.12 $^{+0.22}_{-0.22}$
518	0.46	5.68±0.64	0.04±0.04	266.66±29.53	0.05±0.0	46.56±5.24	0.07±0.01	1.24±0.14	0.09±0.01	-0.18	0.08	-0.08±0.05	43.91±0.0	3321.98±900.62	0.0±0.0	7.96 $^{+0.44}_{-0.44}$
541	0.44	3.21±0.37	0.03±0.05	122.05±13.74	0.11±0.01	37.49±4.28	0.11±0.01	1.08±0.13	0.12±0.01	0.19	0.07	0.21±0.08	44.11±0.0	3245.29±111.17	1.52±0.07	7.49 $^{+0.24}_{-0.24}$
645	0.47	8.94±1.44	0.52±0.76	453.81±50.61	0.06±0.0	37.09±4.6	0.47±0.04	2.28±0.26	0.1±0.01	-0.8	0.0	-3.18±0.08	44.11±0.0	4259.19±90.47	0.4±0.01	7.74 $^{+0.03}_{-0.1}$
720	0.47	5.58±0.66	0.11±0.05	677.02±77.4	0.08±0.01	119.07±13.81	0.14±0.01	3.68±0.45	0.08±0.01	-0.4	0.0	-0.42±0.03	44.3±0.0	3405.89±22.33	0.52±0.01	7.91 $^{+0.23}_{-0.13}$
733	0.46	4.77±0.55	0.07±0.04	389.41±44.72	0.1±0.01	80.97±9.26	0.1±0.01	1.96±0.23	0.11±0.01	-0.02	0.83	0.05±0.03	43.86±0.0	4689.79±44.47	0.6±0.02	8.13 $^{+0.21}_{-0.21}$
766	0.16	2.44±0.28	0.08±0.02	1494.08±165.3	0.07±0.01	601.35±67.42	0.09±0.01	21.19±2.75	0.07±0.01	0.12	0.27	0.06±0.02	43.73±0.0	1936.26±7.28	1.45±0.01	7.14 $^{+0.2}_{-0.2}$
767	0.53	8.81±2.73	-	110.39±25.11	0.02±0.0	8.26±2.13	0.5±0.12	1.02±0.23	0.07±0.01	-0.65	0.0	-1.52±1.36	43.93±0.0	2003.55±3868.39	0.0±0.0	7.53 $^{+1.88}_{-1.88}$
768	0.26	3.95±0.47	0.09±0.03	959.57±105.6	0.17±0.01	233.07±26.53	0.18±0.01	6.21±0.81	0.1±0.01	-0.49	0.0	-0.42±0.02	43.31±0.0	9093.06±611.77	0.53±0.02	8.45 $^{+0.26}_{-0.26}$
769	0.19	5.25±0.85	-	249.68±28.19	0.16±0.01	37.75±4.82	0.5±0.04	5.51±0.72	0.09±0.01	-0.71	0.0	-1.12±0.12	42.97±0.0	6250.34±124.45	1.05±0.02	7.87 $^{+0.22}_{-0.22}$
772	0.25	4.52±0.66	0.42±0.23	454.49±49.76	0.12±0.01	74.52±8.66	0.46±0.03	5.48±0.63	0.07±0.01	-0.54	0.0	-2.53±0.06	43.44±0.0	3089.67±65.88	0.67±0.02	6.72 $^{+0.15}_{-0.15}$
775	0.17	3.5±0.39	0.08±0.02	1489.45±166.07	0.08±0.01	411.82±45.64	0.13±0.01	13.54±1.66	0.06±0.0	-0.19	0.08	-0.27±0.03	43.54±0.0	3662.02±26.73	0.73±0.01	7.84 $^{+0.53}_{-0.27}$
776	0.12	4.39±0.56	0.28±0.11	1275.48±140.8	0.11±0.01	265.29±30.33	0.29±0.02	12.09±1.48	0.12±0.01	-0.64	0.0	-0.9±0.03	43.12±0.0	4344.84±557.6	0.78±0.04	7.43 $^{+0.06}_{-0.14}$
779	0.15	3.53±0.41	0.07±0.02	767.31±86.9	0.1±0.01	213.23±24.35	0.09±0.01	4.81±0.57	0.08±0.01	-0.05	0.64	-0.14±0.02	43.09±0.0	2944.79±20.28	0.57±0.01	7.34 $^{+0.04}_{-0.08}$
781	0.26	3.19±0.36	0.05±0.01	570.41±63.34	0.06±0.0	178.32±20.09	0.08±0.01	4.59±0.56	0.09±0.01	-0.43	0.0	-0.26±0.02	43.6±0.02	2989.96±48.32	0.59±0.04	8.06 $^{+0.04}_{-0.04}$
782	0.36	3.54±0.41	0.03±0.07	444.06±52.26	0.18±0.01	124.07±14.35	0.21±0.02	4.4±0.63	0.17±0.01	-0.56	0.0	-0.41±0.02	43.91±0.0	3428.09±36.56	1.03±0.02	7.67 $^{+0.04}_{-0.1}$
789	0.42	3.14±0.36	0.09±0.03	263.38±30.0	0.07±0.01	82.37±9.38	0.12±0.01	1.55±0.18	0.08±0.01	-0.33	0.0	-0.5±0.05	43.68±0.0	4148.68±70.17	0.55±0.02	7.94 $^{+0.22}_{-0.22}$
790	0.24	3.29±0.38	0.08±0.02	770.02±88.43	0.11±0.01	235.63±26.97	0.12±0.01	6.57±0.82	0.07±0.01	-0.08	0.47	-0.09±0.03	43.26±0.0	9207.55±268.85	0.66±0.04	8.45 $^{+0.68}_{-0.25}$
792	0.53	6.54±0.27	-	50.53±9.13	0.09±0.02	3.82±4.2	0.47±0.09	0.87±0.25	0.09±0.01	-0.05	0.7	-1.2±0.47	43.0±0.01	5111.22±823.91	0.81±0.09	7.75 $^{+0.34}_{-0.34}$
797	0.24	2.21±0.36	0.09±0.02	79.38±47.06	0.08±0.01	35.47±15.43	0.14±0.01	2.11±0.48	0.05±0.0	-0.1	0.36	-0.18±0.12	43.14±0.0	1474.1±47.1	1.7±0.03	6.58 $^{+0.23}_{-0.23}$
798	0.42	3.08±0.26	0.04±0.01	407.92±18.47	0.06±0.01	131.24±8.19	0.05±0.0	3.69±0.53	0.08±0.01	0.07	0.51	0.07±0.03	44.05±0.0	2311.19±62.02	1.13±0.06	7.5 $^{+0.23}_{-0.23}$
822	0.29	2.32±0.38	0.1±0.03	185.84±50.08	0.27±0.02	74.47±17.02	0.26±0.02	4.46±0.66	0.16±0.01	0.03	0.81	-0.02±0.07	43.6±0.0	1847.81±63.39	1.47±0.05	7.03 $^{+0.23}_{-0.23}$
840	0.24	3.37±1.48	0.09±0.03	534.45±11.65	0.19±0.01	152.26±1.24	0.17±0.01	5.21±0.41	0.12±0.01	0.37	0.0	0.18±0.02	43.18±0.0	7409.47±113.24	1.05±0.02	8.11 $^{+0.2}_{-0.18}$
845	0.27	5.57±1.5	-	83.07±6.54	0.17±0.02	7.06±0.57	0.72±0.11	2.63±0.11	0.1±0.01	0.2	0.15	1.94±0.62	42.73±0.01	9023.24±930.44	0.87±0.07	8.1 $^{+0.29}_{-0.29}$
846	0.23	3.48±0.93	-	13.72±2.17	0.18±0.03	1.85±0.34	0.49±0.12	0.34±0.05	0.19±0.02	-0.23	0.13	0.31±0.34	41.83±0.01	3464.89±1038.81	0.0±0.0	7.0 $^{+0.46}_{-0.46}$

